NUMERICAL SIMULATIONS OF THE FLOW INSIDE AN S-SHAPED INTAKE DIFFUSER

A.L. Vuillerme, S. Deck
Office National d'Etudes et de Recherches Aérospatiales (ONERA), Châtillon, France

R. Chevrier
MBDA, Châtillon, France

Introduction

The current trend in the design of missiles or combat aircraft is to reduce costs and to enhance the stealth. Hence the intake integration becomes an increasingly important issue. In particular shortened and highly curved S-shaped inlets are beneficial to reduce the vehicle size and to shield the engine face from direct observation. Nevertheless they involve an increase of pressure loss and flow distortion detrimental to the engine operability.

In the framework of CAMSA study (Aerodynamic Conception of Subsonic Air-breathing Missiles) supported by the French MoD (DGA), the ability to capture the main flow features was evaluated by various codes and turbulence modelling (RANS and DES). The study focused on the HRW S-duct, tested at NASA Lewis Research Center and representative of a generic intake diffuser [1]. This test-case constitutes a complex configuration featuring a large separated flow region very difficult to accurately predict by CFD.

In this paper, we first detail the test-case and the numerical methodologies developed and used to handle this class of problem. Then we focus on validation through comparisons with available experimental data.

Test-case description

The geometry of the test-case is presented in figure 1.

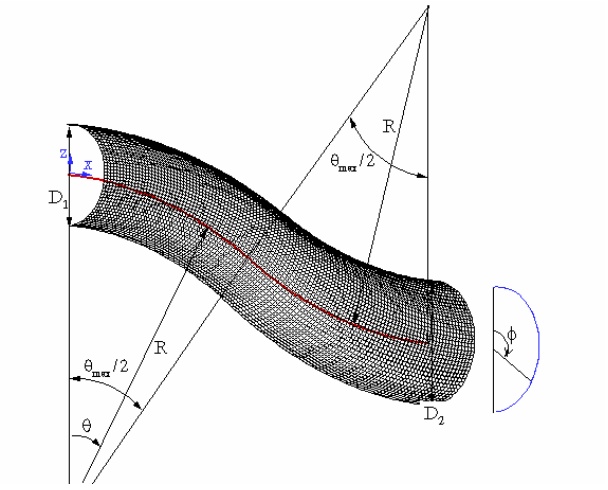

Fig. 1. Geometry of the test-case

The duct centerline is defined by two $\theta_{max}/2=30^o$ arcs with an identical radius of curvature of R=1.02m. The (x_{cl}, y_{cl}, z_{cl},) coordinates of the duct centerline are given by equations (1a) and (1b). The cross-sectional shape of the duct perpendicular to the centerline is circular. The radius of the cross-section varies with the arc angle θ and is given by equation (2), in which D_1 and D_2 are respectively the inlet and outlet duct diameters. The values used for construction are D_1=0.2042m and D_2=0.2544m, which provides an area ratio of 1.52. The offset of the duct resulting from centerline curvature is $1.34D_1$ and the length of the duct measured along the centerline is $5.23D_1$.

$$For\ 0 \le \theta \le \frac{\theta_{max}}{2}: \qquad (1a)$$

$$x_{cl} = R\sin(\theta);\quad y_{cl} = 0;\quad z_{cl} = R\cos(\theta) - R$$

$$For\ \frac{\theta_{max}}{2} \le \theta \le \theta_{max}: \qquad (1b)$$

$$x_{cl} = 2R\sin\left(\frac{\theta_{max}}{2}\right) - R\sin(\theta_{max} - \theta);\ y_{cl} = 0;$$

$$z_{cl} = 2R\cos\left(\frac{\theta_{max}}{2}\right) - R - R\cos(\theta_{max} - \theta)$$

$$\frac{2r}{D_1} = 1 + 3\left(\frac{D_2}{D_1} - 1\right)\left(\frac{\theta}{\theta_{max}}\right)^2 - 2\left(\frac{D_2}{D_1} - 1\right)\left(\frac{\theta}{\theta_{max}}\right)^3 \qquad (2)$$

For the experiment, the inlet total pressure and total temperature are respectively 115400 Pa and 308.7 K. At s/D_1=-0.5, half an inlet diameter upstream from the duct inlet, the Mach number is 0.6 and the boundary layer thickness is approximately 4% of the duct inlet diameter. The test-case flow conditions correspond to a mass-flow of 7.135 kg/s and a Reynolds number based on the inlet diameter of $Re_{D1}=2.6\ 10^6$.

The data available from the experiment include wall static pressures along three azimuthal angles ($\phi=10^o$, 90^o, and 170^o) and Mach and total-pressure contours at the engine face (s/D_1=5.73, "s" being the curvilinear abscissa). The total (Pi) and static (Ps) pressures are presented as pressure coefficients given by the following equations:

$$Cp = \frac{Ps - Ps_1}{Pi_1 - Ps_1},\ CPi = \frac{Pi - Ps_1}{Pi_1 - Ps_1} \qquad (3)$$

where Pi_1 and Ps_1 are respectively the inlet total pressure on the centerline and the inlet wall static pressure measured at $\phi=180^o$, one radius upstream from the S-duct inlet (i.e. s/D_1=-0.5).

Thus, the degree of success of the computations in predicting the flow is judged against the wall static pressure coefficient distributions along the curvilinear abscissa on the one hand, and the Mach number and CPi contours in the CEP (Compressor Entry Plane) on the other hand.

In a second step, the performance of the intake is evaluated through overall coefficients such as pressure recovery and distortion coefficient DC60. In this study, the pressure recovery η_{02} is defined as:

$$\eta_{02} = \frac{Pi_2}{Pi_1} \qquad (4)$$

where Pi_2 is the average total pressure weighted by the mass-flow at s/D_1=5.73 and Pi_1 is the inlet total pressure. The parameter *DC60* is defined by:

$$DC60 = \frac{Pi_2 - Pi_{2,60\,min}}{Q_2} \qquad (5)$$

where $Pi_{2,60min}$ is the average total pressure weighted by the mass-flow at the worst 60 deg sector of engine face and Q_2 is the average dynamic head weighted by the mass-flow at engine face. After having scanned and post-processed the experimental data supplied in ref. [1], the following values were obtained:

$$\eta_{02\,exp.} = 0.971 \quad \text{and} \quad DC60_{\,exp.} = 0.358 \qquad (6)$$

Numerical methods

Three different in-house codes were used to calculate the flow inside the S-duct: AEROLOG by MBDA, FLU3M and elsA [2]

by ONERA. These solvers are cell-centred finite volume software solving the three-dimensional RANS equations on multi-block structured grids. Turbulence can be modelled by the algebraic turbulence model of Baldwin-Lomax (BL), by the one-equation model of Spalart-Allmaras (SA), or by a wide variety of two-equation models among which the most popular ones such as the k-l model of Smith, the k-ε models of Jones-Launder (JL) or Chien, or a number of k-ω models. Furthermore, several explicit algebraic Reynolds stress models have recently been implemented in elsA, in Wallin-Johansson (WJ) [3] and Shi-Zhu-Lumley (SZL) [4] formulations.

In the elsA code, the Navier-Stokes equations and the turbulence transport equations are solved separately. Indeed the RANS equations can be solved either with Jameson centred-scheme using a numeric viscosity with correction of Martinelli or with a Roe type upwind scheme, whereas a Roe scheme is necessarily used to solve the turbulence transport equations. For the time integration, a four-step Runge-Kutta scheme may be used associated with the Implicit Residual Smoothing (IRS) method or a backward-Euler scheme preferably associated with LU-RELAX or LU-SSOR implicit methods.

Among hybrid strategies, the approach that has probably drawn most attention is the Detached Eddy Simulation (DES) which was proposed by Spalart et al. [5] in 1997. This method has given encouraging results for a wide range of flows exhibiting massive separation [6] [7] [8] [9] and has since gone through various stages of refinement. The reader is referred to Spalart [10] for current status and perspectives in Detached Eddy Simulation.

The model implemented in the FLU3M code was originally based on the Spalart-Allmaras RANS model which solves a one-equation turbulence model for the pseudo-eddy viscosity $\tilde{\upsilon}$:

$$\frac{D\tilde{\upsilon}}{Dt} = c_{b1}\tilde{S}\tilde{\upsilon} + \frac{1}{\sigma}\left(\nabla.\left((\upsilon+\tilde{\upsilon})\nabla\tilde{\upsilon}\right) + c_{b2}(\nabla\tilde{\upsilon})^2\right) - c_{w1}f_w\left(\frac{\tilde{\upsilon}}{d}\right)^2 \quad (3)$$

The eddy viscosity is defined by:

$$\mu_t = \rho\tilde{\upsilon}f_{v1},\ f_{v1} = \frac{\chi^3}{\chi^3 + c_{v1}^3},\ \chi = \frac{\tilde{\upsilon}}{\upsilon} \quad (4)$$

The f_w and f_{v1} functions are near-wall damping functions of the model and we refer to the original paper [11] for details on the constants and the quantities involved. What is important here is that the model is provided with a destruction term for the eddy viscosity that contains d, the distance to the closest wall. This term when balanced with the production term adjusts the eddy viscosity to scale with the local deformation rate $\tilde{S}$ producing an eddy viscosity given by:

$$\tilde{\upsilon} \propto \tilde{S}d^2 . \quad (5)$$

Following these arguments, Spalart et al. suggested to replace d with the new length scale $\tilde{d}$ given by:

$$\tilde{d} = \min\left(d, C_{DES}\Delta\right) with\ \Delta = \max\left(\Delta_x, \Delta_y, \Delta_z\right) \quad (6)$$

where Δ is the computational mesh size. Indeed, in the attached boundary layer, due to the significant grid anisotropy ($\Delta_x \sim \Delta_z >> \Delta_y$) typical of this flow region, $\tilde{d} = d$ and the model reduces to the standard SA RANS model. Otherwise, once a field point is far enough from walls ($d > C_{DES}\Delta$), the length scale of the model performs as a Smagorinsky like subgrid-scale version of the SA model.

However, standard DES introduces a significant dependency on the RANS part of the simulation which requires a grid spacing for the wall grid in tangential direction larger than the boundary layer thickness at that location. This grid resolution may be easily violated inside the duct. If the switching to LES mode occurs inside the RANS boundary layer, this will result in an underestimation of the skin friction coefficient [12][13]. To avoid this problem, we used a “zonal-DES”[14]

method where attached boundary layer regions are explicitly treated in RANS mode whatever the grid resolution.

Results and discussion

Because of the symmetry of the intake, grids were constructed only for half the model using two blocks of O+H topology with either 275 000, 700 000 or 1 700 000 cells. Two circular cylinder extensions were attached upstream and downstream of the S-duct to reach the appropriate boundary layer thickness at the inlet and to apply the boundary conditions far from the sections of interest.

This paper is divided into three main sections. The first part is dedicated to a turbulence model influence performed in an industrial context, whose aim is to rapidly assess the intake performance without precisely describing the local flow features. In a second part, in order to improve the flow field prediction, a grid sensitivity as well as a turbulence model influence are presented using classical and state-of-the-art turbulence modelling. In a last part the benefit of a hybrid RANS/LES approach in capturing the flow physics is detailed.

Industrial approach

The purpose of this first part is to assess the ability to capture the flow features in the frame of an industrial approach. In order to keep a reasonable computational time for a complete missile or aircraft simulation, manufacturers cannot afford extremely large grids. Hence a “coarse” mesh of approximately 275,000 nodes is commonly used to model intake diffusers, only half of the configuration being considered.

To illustrate the flow characteristics inside the S-shaped diffuser, figure 2 presents the computed Mach number and CPi contours and clearly shows the separated flow region inside the S-bend.

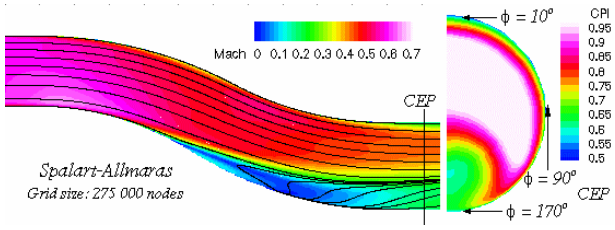

Fig. 2. Mach number and CPi contours in the symmetry plane and at the engine face

Figure 3 then summarises different computations performed with various turbulence models commonly used such as the Baldwin-Lomax (BL), Spalart-Allmaras (SA) and k-l Smith ones. Results obtained with the k-kl model [15] (using the Boussinesq assumption for the shear stresses) are also reported in the graphs. One first notices that each computation predicts the pressure recovery within 1.5%, which is acceptable from an industrial point of view. Nevertheless, in term of flow distortion, one may notice that large result discrepancies are obtained around the experimental DC60 value. Differences between computations and experiment can reach 50%, the best agreement being obtained with the Baldwin-Lomax turbulence model.

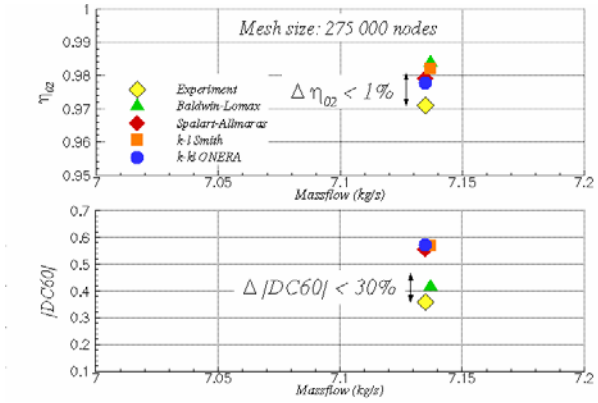

Fig. 3. Performance of the S-duct

Once the overall characteristics have been calculated, it is essential to compare the local flow field with the experiment in order to evaluate the accuracy of each computation and to identify the reasons for the differences. Firstly the Mach number contours at the engine face (figure 4) highlight a low-energy area of fluid on the lower duct portion coming from the boundary layer separation. This low-

velocity region corresponds to a low total pressure core which is responsible for the high flow distortion. Concerning the lateral extension of the low-speed region, a rather good agreement with experimental data is obtained with the SA and k-kl turbulence models, whilst the algebraic model yields a too narrow one. It is also worth noting the underestimation of the Mach number levels in the core region, which leads to the overestimation of the distortion parameter by the SA and k-kl models. One lastly notices that each turbulence modelling under-predict the cross stream gradient downstream from the recirculation region. On the other hand, comparisons of the wall static pressure distributions at ϕ=90^o and 170^o (figure 5) indicate the separation point is rather well predicted by each computation. The experimental "plateau" region corresponding to the separated flow area is slightly pronounced with the SA and k-kl models. Conversely the BL overestimates its longitudinal extent as well as its level.

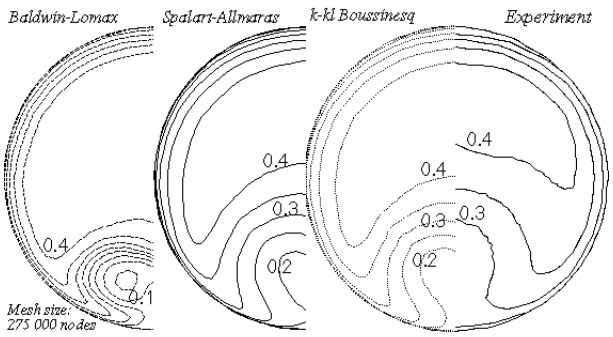

Fig. 4. Mach number contours in the CEP

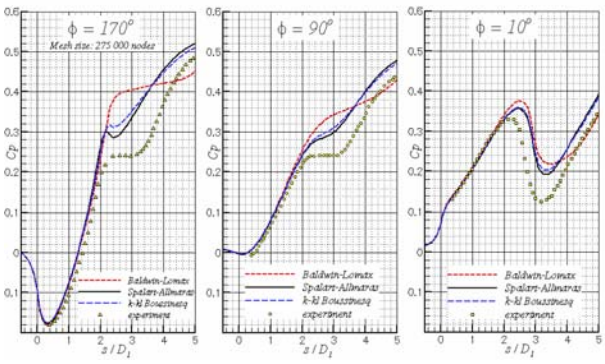

Fig. 5. Comparison of the Cp distributions

To conclude this computational work performed in an industrial context, the restitution of the flow characteristics appears acceptable in term of efficiency, whereas the flow topology is not accurately predicted by CFD, which leads to a poor prediction of the engine face flow distortion. It is also worth noting that the algebraic model of Baldwin-Lomax, which well reproduces the S-duct performance, predicts a local flow field far from the experiment. As a result, the following part is concerned with the studies of grid resolution and turbulence modelling influences, the target being to improve the prediction of the local flow field.

Grid and turbulence model influences

Because each numerical result is an approximate solution of non-linear partial differential equations, there exist truncation errors in the flow domains which depend on the grid resolution. Hence it is important to decide whether the mesh size is sufficient to accurately solve the Navier-Stokes equations. A grid sensitivity analysis is therefore necessary. For this purpose a sequence of three grids of increasing resolution has been built; they are named coarse, medium and fine grid in the following. Figure 6 summarises the performance of the S-bend diffuser (pressure recovery and flow distortion coefficient) calculated for each grid using the BL, SA and k-kl EARSM [16] turbulence models. As expected, the finer the grid is, the better the prediction of the distortion parameter is. This comes from the fact that total pressure maps are closer to experiment when the grid is refined, as illustrated on figure 7 plotting the CPi contours in the CEP.

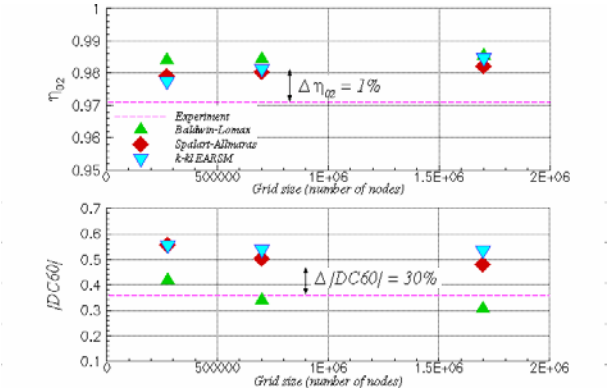

Fig. 6. Comparison of the inlet performance according to the mesh size

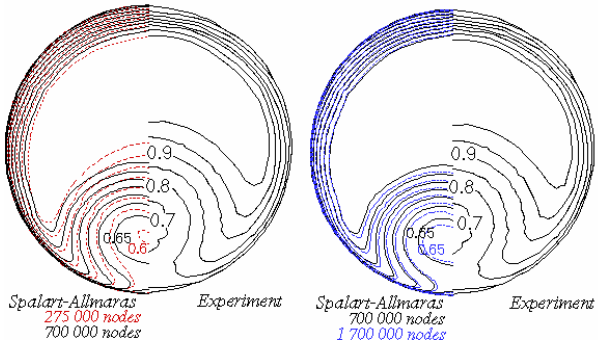

Fig. 7. Comparison of the CPi contours in the CEP according to the mesh size

The grid effect is also evaluated through the CP distributions along three azimuthal positions. Figure 8 shows that a medium mesh of 700 000 nodes already gives an accurate prediction of the pressure distributions in the separated flow region. The constant static pressure area which is characteristic of the recirculation region is indeed well predicted at ϕ=90° and 170°.

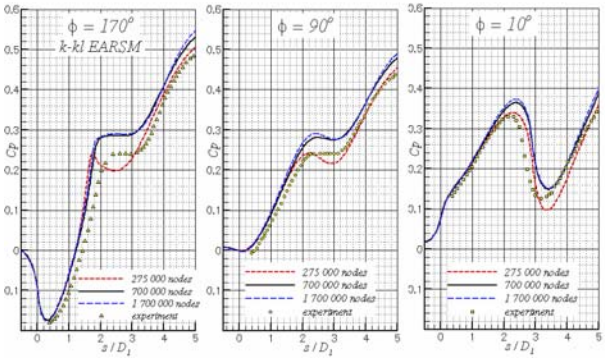

Fig. 8. Comparison of the Cp distributions according to the mesh size

As a result, the medium grid of 700 000 nodes is used in the subsequent computations since it allows a reasonable trade-off between the quality of the flow solution and the computational time.

With the view of assessing innovative turbulence modelling, a number of additional computations have been performed. More precisely EARSM models (Explicit Algebraic Reynolds Stress Models), based on either the k-ε JL, k-ε Chien or ONERA k-kl [16] ones, have been used to check the effect of taking into account the turbulence anisotropy. In the following figures, EARSM results are compared with those obtained with other models such as the SA and the k-kl ones [15].

Figure 9 gives an overall view of predicted values of the S-duct performance. In particular the graph highlights the improvement of the flow distortion prediction when using the EARSM formulation instead of the Boussinesq one in the case of the ONERA k-kl model. On the other hand we notice that the pressure recovery is predicted within 1% from the experimental value whatever the EARSM model considered. However the distortion parameter is still definitely higher than the experimental value. This difference comes from the under-prediction of the total pressure level downstream from the recirculation region as illustrated on figure 10. Concerning the extent of the low-energy area, the best agreement with experimental data is obtained with the k-kl EARSM model (figures 10 and 11).

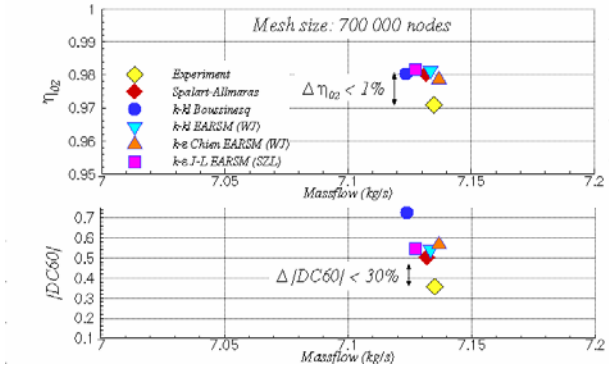

Fig. 9. Comparison of the inlet performance according to the turbulence model

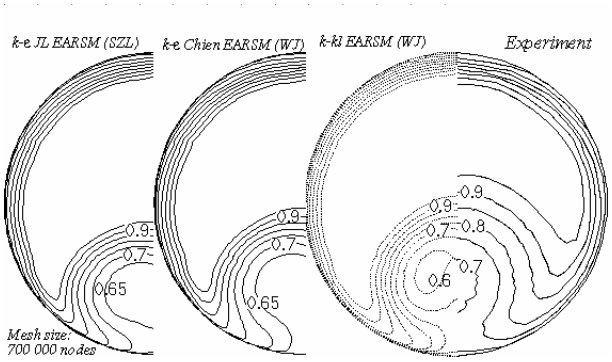

Fig. 10. Comparison of the iso-CPi contours in the CEP according to the turbulence model

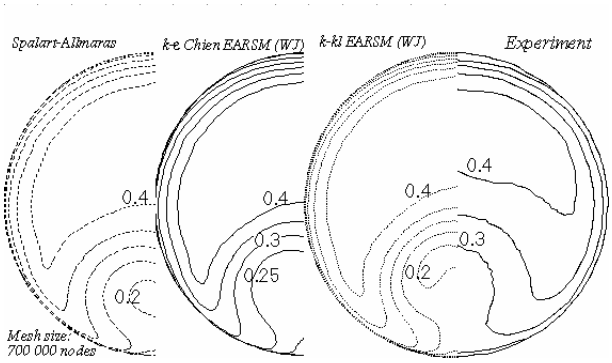

Fig. 11. Comparison of the iso-Mach contours in the CEP according to the turbulence model

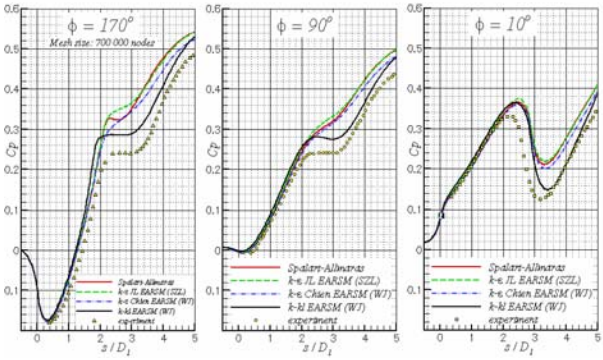

Fig. 12. Comparison of the CP distributions according to the turbulence model

The static pressure distributions along the S-bend are compared on figure 12. Firstly one notes that both k-ε Chien and JL EARSM models do not exhibit the experimental plateau region in the S-duct curve. On the other hand the computation performed with the k-kl EARSM model shows a quite remarkable agreement with experiment concerning the longitudinal extent of the constant pressure area. As a result this latter model seems to be very appropriate for simulating the local flow field with a RANS approach.

The grid and turbulence model influences enabled us to determine the appropriate mesh refinement and turbulence modelling for a RANS type method. However it appears that several flow features are not adequately captured, leading to a miss-prediction of the flow distortion in the CEP. Thus it was decided to evaluate a hybrid approach, offering the potential to combine the accuracy of the LES and the cost-effectiveness of the RANS methods.

Assessment of a hybrid method

The grid used for the DES computation (figure 13) contains 7 domains. Three of them are treated in DES mode, while the others are explicitly handled in URANS mode. In addition the “gray-area” is locally forced in the DES domains in order to shield the attached boundary layer. The mesh globally consists of 4 million nodes.

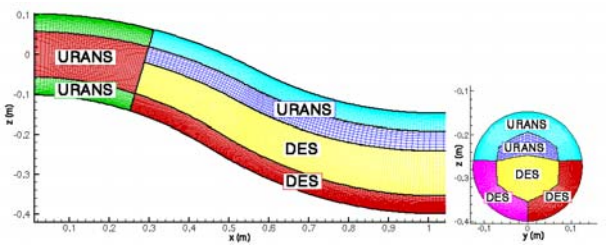

Fig. 13. Patch-grid

At first, a preliminary RANS computation was performed on the patch-grid in order to check the symmetry of the steady solution and the continuity between non-coincident blocks, as illustrated in figure 14. Furthermore the skin friction lines on the lower part of the S-duct clearly show the extent of the separated region.

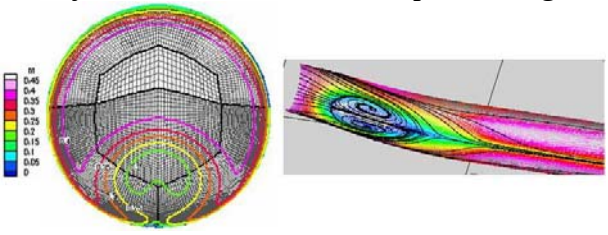

Fig. 14. Mach contours in the CEP and friction lines (RANS computation)

Figure 15 gives an insight into the turbulent nature of the instantaneous flow field. One can especially notice the large vortices being formed in the shear layer and impacting the wall in the reattachment region.

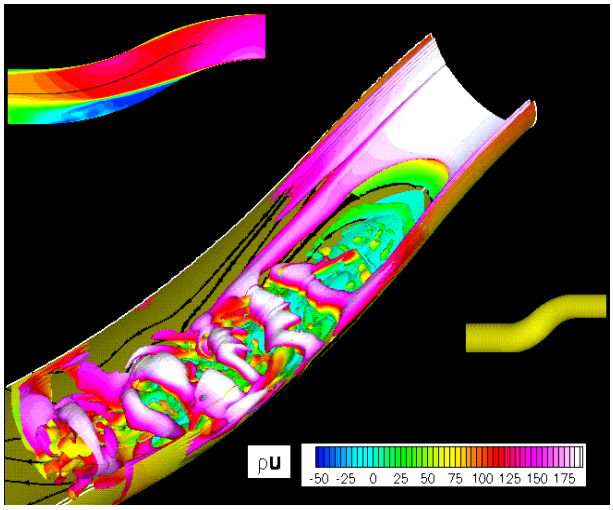

Fig. 15. Turbulent structures in the recirculation region

The DES aerodynamic fields are time-averaged during computation before being compared with the experiment and with RANS SA and k-kl EARSM computations. First of all, the Mach number and CPi contours in the CEP (figures 16 and 17) show that the DES calculation predicts much more accurately the lateral extent of the low-speed region, the radial flow diffusion and the resulting distortion coefficient. This certainly comes from the fact that coherent structures are taken into account. Moreover, the location of the separation is correctly determined by both RANS and DES computations, as shown on figure 18 representing the Cp distributions along the three azimuthal positions. However the length of the constant pressure area, characteristic of the recirculation region, is better predicted by the DES approach than by the RANS one. Indeed, as can be seen at ϕ = 90° and 170°, the DES method improves the prediction of the longitudinal and circumferential extents of the separated flow region. Concerning the overall coefficients, the pressure recovery is calculated within 1% by all computations (RANS and DES). However the distortion parameter which is extremely sensitive to the local flow characteristics is systematically over-estimated, the deviation from the experimental value being lower for the DES solution than for the RANS ones.

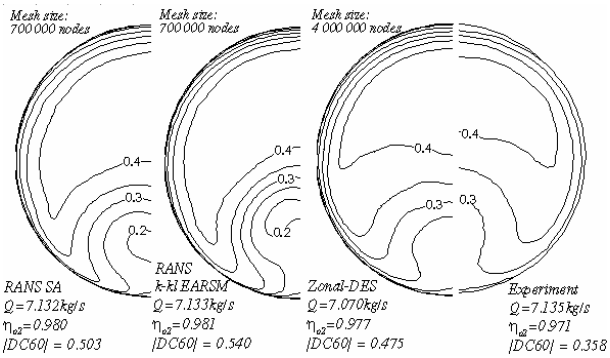

Fig. 16. Iso-Mach contours in the CEP

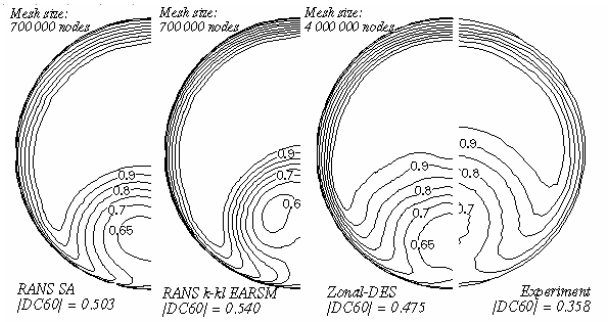

Fig. 17. Iso-CPi contours in the CEP

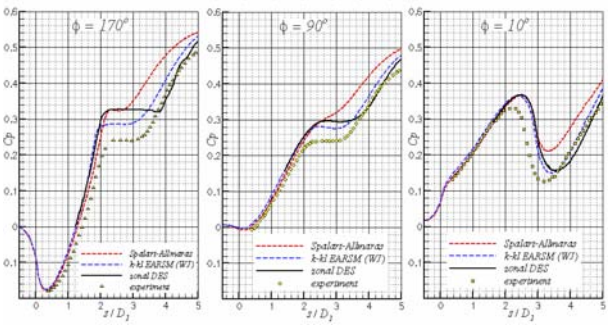

Fig. 18. Cp distributions along the duct

Beyond the time-averaged flow features, the DES approach offers the possibility to capture the unsteadiness and the time-evolution of the flow field. As an example, figure 19, which provides an instantaneous Schlieren-like visualisation ($\|\nabla\rho\|$) in the vicinity of the separated area, illustrates the complexity of the flow pattern during the reattachment process. One can firstly notice the roll up of two-dimensional eddies. In addition, after the reattachment process, some

large scale structures are convected towards the CEP, whilst smaller structures are carried back towards the separated area leading to a feedback mechanism. On the same figure, the time-history of the fluctuation of the transverse velocity component is plotted for a sensor situated close to the engine face. It is worth noting the highly 3-dimensional and turbulent behaviour of the reattachment process, since the averaged turbulent rate is 11%.

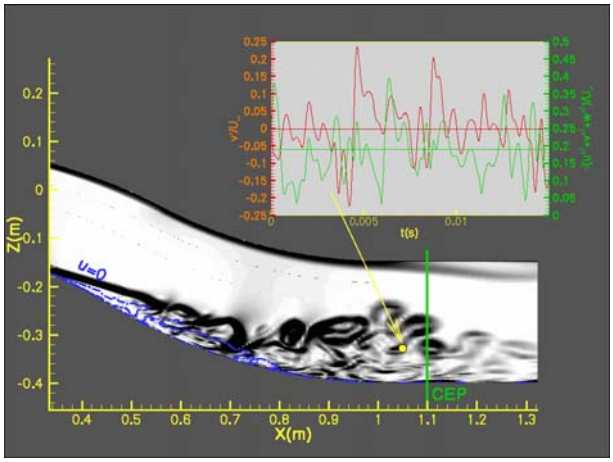

Fig. 19. Schlieren-like visualisation and time history of a velocity component

Figure 20 finally displays the rms level of the fluctuating pressure in the CEP, expressed in Pascal and in sound pressure levels. The largest Prms values (of the order of 150 dB, i.e. 5% of the dynamic pressure) are observed downstream from the recirculation region (see also figure 19). These high levels highlight the unsteady nature of the flow arriving in the CEP.

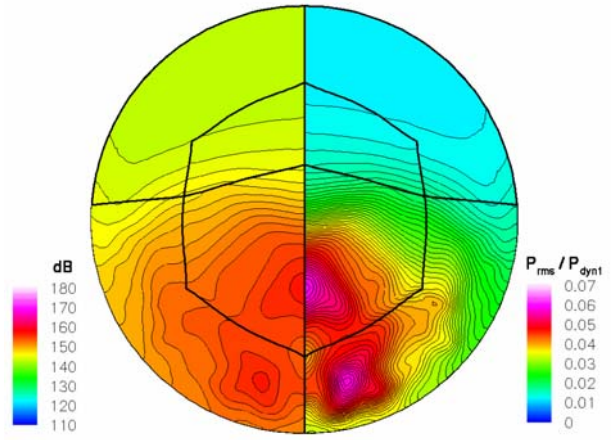

Fig. 20. Prms and corresponding sound pressure levels in the CEP

As a result the DES computation has demonstrated the ability of the method to handle separated flow inside an S-shaped intake diffuser. Not only does it improve the mean flow field prediction but it also gives access to large-scale time-dependant flow features and to unsteady total pressure distortion.

Conclusion

The present study was conducted to evaluate the capabilities of the Computational Fluid Dynamics methods to model the flow physics and performance characteristics of a diffusing subsonic S-duct. This was done by solving the full three-dimensional Navier-Stokes equations coupled with various turbulence models, by performing a Detached Eddy Simulation and by comparing the numerical results with experimental data. The global flow features are generally correctly captured by RANS computations. The DES approach offers the possibility to model the large-scale time-dependent features of the flow and to predict the time-variant total pressure distortion. It also delivers more accurate predictions of the mean flow properties.

Acknowledgment

The authors gratefully acknowledge the DGA from the French Ministry of Defence which granted the research reported in this paper.

References

[1] Harloff G.J., Reichert B.A., Wellborn S.R. *Navier-Stokes Analysis and Experimental Data Comparison of Compressible Flow in a Diffusing S-Duct.* AIAA-92-2699-CP, 1992.

[2] Gazaix M., Jolles A., Lazareff M. *The elsA Object-Oriented Computational Tool for Industrial Applications.* 23rd Congress of ICAS, Toronto, Canada. September 8-13, 2002.

[3] S. Wallin and A.V. Johansson. *An explicit algebraic Reynolds stress model for incompressible and compressible turbulent flows*. Journal of Fluid Mechanics, 403: 89-132, 2000.

[4] T. Shih, J. Zhu, J. Lumley. *A realisable Reynolds stress algebraic equation model.* TM 105993 – ICOMP 92-27, CMOTT 92-14 – NASA, 1992.

[5] P.R. Spalart, W.H. Jou, M. Strelets, and S.R., Allmaras. *Comments on the feasibility of LES for wings and on a hybrid RANS/LES approach.* In Proceedings pp 137-147, 1st AFSOR Int. Conf. on DNS, Ruston, 1998.

[6] K.D. Squires, J.R. Forsythe, S.A. Morton, W.Z. Strang, K.E. Wurtzler, R.F. Tomarao, M.J. Grismer and P.R. Spalart. *Progress on Detached-Eddy Simulation of Massively Separated Flows.* AIAA paper 02-0591, Reno, Jan. 2002.

[7] M. Strelets. *Detached Eddy Simulation of Massively Separated Flows.* AIAA paper 01-0879, Reno, Jan. 2001.

[8] J.R. Forsythe, K.D. Squires, K.E. Wurtzler and P.R. Spalart. *Detached Eddy-Simulation of Fighter Aircraft at High_Alpha.* AIAA paper 02-0591, Reno, Jan. 2002.

[9] S. Deck, E. Garnier and Ph. Guillen. *Turbulence modelling applied to space launcher configurations.* Journal of Turbulence, vol.3, (57), pp1-21, Dec. 2002.

[10] P.R. Spalart. *Topics in Detached Eddy Simulation.* ICCFD3, Toronto, Canada, July 2004.

[11] P.R. Spalart, S.R. Allmaras. *A one equation turbulence model for aerodynamic flows*. La Recherche Aérospatiale, pp 5-21, 1994.

[12] N.V. Nikitin, F. Nicoud, B. Wasistho, K.D. Squires. *An approach to wall-modelling in large eddy simulation.* Physics of Fluids, vol.12, pp 1629-1631, 2000.

[13] B. Caruelle. *Simulations d'écoulements instationnaires turbulents en aérodynamique: applications à la prédiction du phénomène de tremblement.* PhD thesis, Institut National Polytechnique de Toulouse, 2000.

[14] S. Deck. *Numerical Simulation of transonic buffet over a supercritical airfoil.* AIAA J., accepted, to appear, 2005.

[15] H. Bézard and T. Daris. *A new kt-ktLt turbulence model for heat flux predictions.* 3rd International Symposium on Turbulence and Shear Flow Phenomena, Sendai, Japan. June 25-27, 2003.

[16] H. Bézard and T. Daris. *Calibrating the length-scale equation with an explicit algebraic Reynolds stress model.* ERCOFTAC International Symposium on Engineering Turbulence Modelling and Experiments - ETMM6. W. Rodi and M. Mulas Editors, ELSEVIER, Sardinia, Italy, May 23-25, 2005.